



# Observations of the Quiet Sun during the Deepest Solar Minimum of the Past Century with Chandrayaan-2 XSM: Elemental Abundances in the Quiescent Corona

Santosh V. Vadawale<sup>1</sup>, Biswajit Mondal<sup>1,2</sup>, N. P. S. Mithun<sup>1,2</sup>, Aweek Sarkar<sup>1</sup>, P. Janardhan<sup>1</sup>, Bhuwan Joshi<sup>1</sup>, Anil Bhardwaj<sup>1</sup>, M. Shanmugam<sup>1</sup>, Arpit R. Patel<sup>1</sup>, Hitesh Kumar L. Adalja<sup>1</sup>, Shiv Kumar Goyal<sup>1</sup>, Tinkal Ladiya<sup>1</sup>, Neeraj Kumar Tiwari<sup>1</sup>, Nishant Singh<sup>1</sup>, and Sushil Kumar<sup>1</sup>

<sup>1</sup>Physical Research Laboratory, Navrangpura, Ahmedabad, Gujarat-380 009, India; [santoshv@prl.res.in](mailto:santoshv@prl.res.in)

<sup>2</sup>Indian Institute of Technology Gandhinagar, Palaj, Gandhinagar, Gujarat-382 355, India

Received 2021 March 1; revised 2021 March 26; accepted 2021 March 30; published 2021 May 4

## Abstract

Elements with low first ionization potential (FIP) are known to be 3–4 times more abundant in active region loops of the solar corona than in the photosphere. There have been observations suggesting that this observed “FIP bias” may be different in other parts of the solar corona and such observations are thus important in understanding the underlying mechanism. The Solar X-ray Monitor (XSM) on board the Chandrayaan-2 mission carried out spectroscopic observations of the Sun in soft X-rays during the 2019–2020 solar minimum, considered to be the quietest solar minimum of the past century. These observations provided a unique opportunity to study soft X-ray spectra of the quiescent solar corona in the absence of any active regions. By modeling high-resolution broadband X-ray spectra from XSM, we estimate the temperature and emission measure during periods of possibly the lowest solar X-ray intensity. We find that the derived parameters remain nearly constant over time with a temperature around 2 MK, suggesting the emission is dominated by X-ray bright points. We also obtain the abundances of Mg, Al, and Si relative to H, and find that the FIP bias is  $\sim 2$ , lower than the values observed in active regions.

*Unified Astronomy Thesaurus concepts:* Quiet sun (1322); Solar abundances (1474)

*Supporting material:* figure set

## 1. Introduction

Knowledge of elemental composition in the solar corona is crucial to understand various outstanding issues, such as energy/mass transfer between different atmospheric layers and the origin of the solar wind. However, it is challenging to measure the absolute elemental abundances (i.e., relative to hydrogen), which leads to a common practice of measuring coronal elemental abundances relative to other elements. One important problem related to the coronal elemental composition is the abundance enhancement of the low first ionization potential (FIP) elements (i.e., elements having FIP less than 10 eV), compared to their photospheric values, often termed as the FIP bias or FIP anomaly. Observations of the FIP anomaly started with the pioneering work of Pottasch (1963). Later, many researchers showed that the abundances of the low FIP elements in the corona can be as much as 3–4 times that of the photosphere (Meyer 1985; Feldman 1992; Fludra & Schmelz 1999; Schmelz et al. 2012). It was also observed that the FIP bias varies within different features of the corona (Feldman & Widing 1993) and shows variation with both the solar cycle and magnetic activity of the Sun (Brooks et al. 2017; Pipin & Tomozov 2018). A detailed review on the topic can be found in Del Zanna & Mason (2018).

While the origin of the FIP bias is not fully understood, recent reports based on the EUV imaging spectroscopy (e.g., Del Zanna 2019; Doschek & Warren 2019) show that the low-temperature ( $\sim 1$  MK) nonactive corona has nearly photospheric abundances. In contrast, hot loops (2–4 MK) at the core of the active region with high magnetic field show stronger (3–4) FIP bias (Feldman 1992; Saba 1995; Feldman & Laming 2000; Feldman & Widing 2003; Del Zanna & Mason 2014). Multiple theories have been proposed in the literature to explain the FIP bias (see Laming 2015 for a review); however, the widely accepted theory is that based

on the ponderomotive force model (Laming 2004, 2009). This model can successfully explain the higher FIP bias in hot, magnetically closed loops as well as photospheric abundances in the relatively cooler open field structures. It also predicts that higher magnetic activity may lead to higher FIP abundance in the solar corona.

Although early visible light solar eclipse observations (Mason 1975) measured coronal abundances relative to hydrogen, most of the XUV spectroscopic observations determine abundances relative to some other elements, such as O or Si. On the other hand, broadband soft X-ray spectroscopic observations are capable of measuring absolute abundances by considering the line to continuum ratio, as initially proposed by Walker (1972) and attempted by Walker et al. (1974a, 1974b). Recently, there have been multiple studies presenting measurement of absolute abundances by self-consistently modeling the continuum and characteristic lines in the observed soft X-ray spectra (e.g., Narendranath et al. 2014, 2020; Warren 2014; Caspi et al. 2015; Dennis et al. 2015; Moore et al. 2018; Schwab et al. 2020). However, these reports are based on observations of solar flares or active regions, where the underlying continuum is easier to measure due to high X-ray flux. Similar studies during quiet-Sun periods have not been possible so far due to very low signal as well as difficulties in measuring the real continuum.

Here we present the first such study of quiet corona using Chandrayaan-2/Solar X-ray Monitor (XSM; Vadawale et al. 2014; Shanmugam et al. 2020), which observes the Sun as a star in the soft X-ray band. These observations carried out during the 2019–2020 solar minimum, believed to be the deepest minimum in the past 100 years (Janardhan et al. 2011, 2015), provided a unique opportunity for long-duration solar X-ray observations in the absence of solar active regions, thereby enabling one to infer the temperature, emission measure, and elemental abundances in

the quiescent solar corona. A companion paper (Vadawale et al. 2021, hereafter Paper II), presents a detailed investigation of the sub-A-class microflares observed in the quiet Sun during this period. The rest of this paper is organized as follows. Section 2 provides the details of observations and data analysis. Results are presented and discussed in Section 3 and finally summarized in Section 4.

## 2. Observations and Data Analysis

Chandrayaan-2 XSM measures the disk-integrated solar X-ray spectra in the energy range of 1–15 keV (Vadawale et al. 2014; Shanmugam et al. 2020). Its primary objective is to provide measurement of incident solar X-ray spectra on the Moon for estimation of elemental abundance on the lunar surface with remote fluorescence spectroscopy. It has been designed to cover the wide intensity range of the solar X-rays all the way from the quiet Sun to X-class solar flares. XSM employs a Silicon Drift Detector to measure the solar spectrum with an energy resolution better than 180 eV at 5.9 keV and a time cadence of 1 s, which is the highest for a broadband solar X-ray spectrometer available so far (Mithun et al. 2020).

The visibility of the Sun varies with two predefined orbital seasons of the Chandrayaan-2 orbiter, namely, “dawn-dusk” (DD) and “noon-midnight” (NM), arising because of the attitude configurations of the spacecraft in the lunar orbit and lasting for about three months each (Vanitha et al. 2020). The primary observing periods for XSM are the DD seasons, typically lasting from mid-February to mid-May and mid-August to mid-November (Mithun et al. 2021b, 2020). In the present work, we use the data from the first two DD seasons from 2019 September 12 to November 20 (DD1) and 2020 February 14 to May 19 (DD2).

The XSM processing electronics generates X-ray spectrum on board at every second. The raw (level-1) XSM data thus consists of 1 s spectra as well as other auxiliary information such as housekeeping parameters and observation geometry, organized as day-wise FITS files. The standard level-2 calibrated data include solar X-ray light curves in the full energy range of 1–15 keV at 1 s cadence and full spectra at a cadence of 60 s. The XSM specific Data Analysis Software (XSMDAS; Mithun et al. 2021a) is used for basic data reduction as well as for generating light curves and spectra with any user-selected time bins greater than 1 s. The only other user input required for analysis is to select good time intervals (GTIs) for the generation of the light curve and spectrum. The default GTI selection includes the conditions for nominal ranges of the instrument health parameters and excludes periods when the Sun angle is greater than  $38^\circ$  or when the Sun is occulted by the Moon. It should be noted that the default condition on the Sun angle considers the radius of the Sun to be  $3 \mathcal{R}_\odot^N$  in order to avoid any partial exposure to the extended corona.

Since the XSM is fixed mounted on the Chandrayaan-2 spacecraft, the position of the Sun within its field of view (FOV) continuously changes throughout the orbit, resulting in a continuous change in the effective area of XSM. The XSMDAS provides two options to account for these variations: it can provide a corrected count rate as if it were observed on-axis, typically used for light curves and time-resolved spectra saved as a type-II PHA file; or the spectra can be retained as

observed counts and the variations of the effective area are accumulated in a corresponding ancillary response file (ARF), typically used for time-integrated spectra saved in a type-I PHA file.

For the present analysis, we use effective area-corrected daily time-resolved spectra for obtaining flux light curves. The time bin size was chosen to be 2 minutes so as to have sufficient counts in each spectra, given the very low X-ray intensity of the Sun. The XSM flux light curve,  $F(t)$ , over any energy range  $E_1$  to  $E_2$  can then be generated from the type-II PHA files  $S(E, t)$  using the equation

$$F(t) = \sum_{E=E_1}^{E_2} \frac{S(E, t) E}{A(E)}, \quad (1)$$

where  $A(E)$  is the on-axis effective area of the XSM. It should be noted that this assumes a diagonal redistribution matrix, which, though not strictly correct, is adequate to estimate flux over broad energy ranges. We then obtained the X-ray flux light curve in the energy range 1.55–12.4 keV (same as the conventional GOES XRS band covering the wavelength range of 1–8 Å) using time-resolved spectra over the first two DD seasons, which is shown in Figure 1.

The flux light curve in Figure 1 clearly shows periods of elevated X-ray intensity due to the presence of active regions on the Sun. The orange background marks the periods when NOAA active regions were present on the solar disk. The pink background marks the periods when NOAA-assigned active regions were not present, but the XSM light curve shows enhancement and corresponding EUV and X-ray images from SDO/AIA and Hinode/X-ray Telescope (XRT), respectively, show bright regions. Since the objective of the present analysis was to focus on the quiet periods, we concentrated only on the periods marked by the blue background in Figure 1 (a detailed analysis of the active region emission will be presented elsewhere). The intervals selected for the present analysis are 2019 September 12–30 and October 14–26 and 2020 February 14–March 7, March 21–29, April 13–23, and May 10–13, spanning a total of 76 days. We find that even during these intervals, when there were no active regions present on the Sun, the XSM light curve shows a number of small flare-like episodes (microflares), which is discussed in Paper II. For the purpose of the spectroscopic investigation of the X-ray emission from a purely quiescent corona, we conservatively ignore such microflares, along with sufficient pre- and post-flare buffer durations, obtained by visual inspection as shown in Figure 2. These identified time intervals were used as user GTIs to generate quiet-Sun spectra for carrying out a detailed spectral analysis.

To perform spectral fitting in XSPEC (Arnaud 1996), we generated XSM spectra (type-I PHA) and ARF for quiet-Sun observations on each of the selected days with the user GTIs corresponding to the nonflaring periods. Three days with very low exposures were ignored from further analysis. The nonsolar background spectrum was obtained using XSM observations when the Sun was outside its FOV. Spectra below 1.3 keV were not used in fitting due to uncertainties in the response for the observations used in the present work (Mithun et al. 2020). For spectral fitting, we use an isothermal plasma emission model generated using the CHIANTI atomic database version 9.0.1 (Dere et al. 1997, 2019), which consists of the continuum

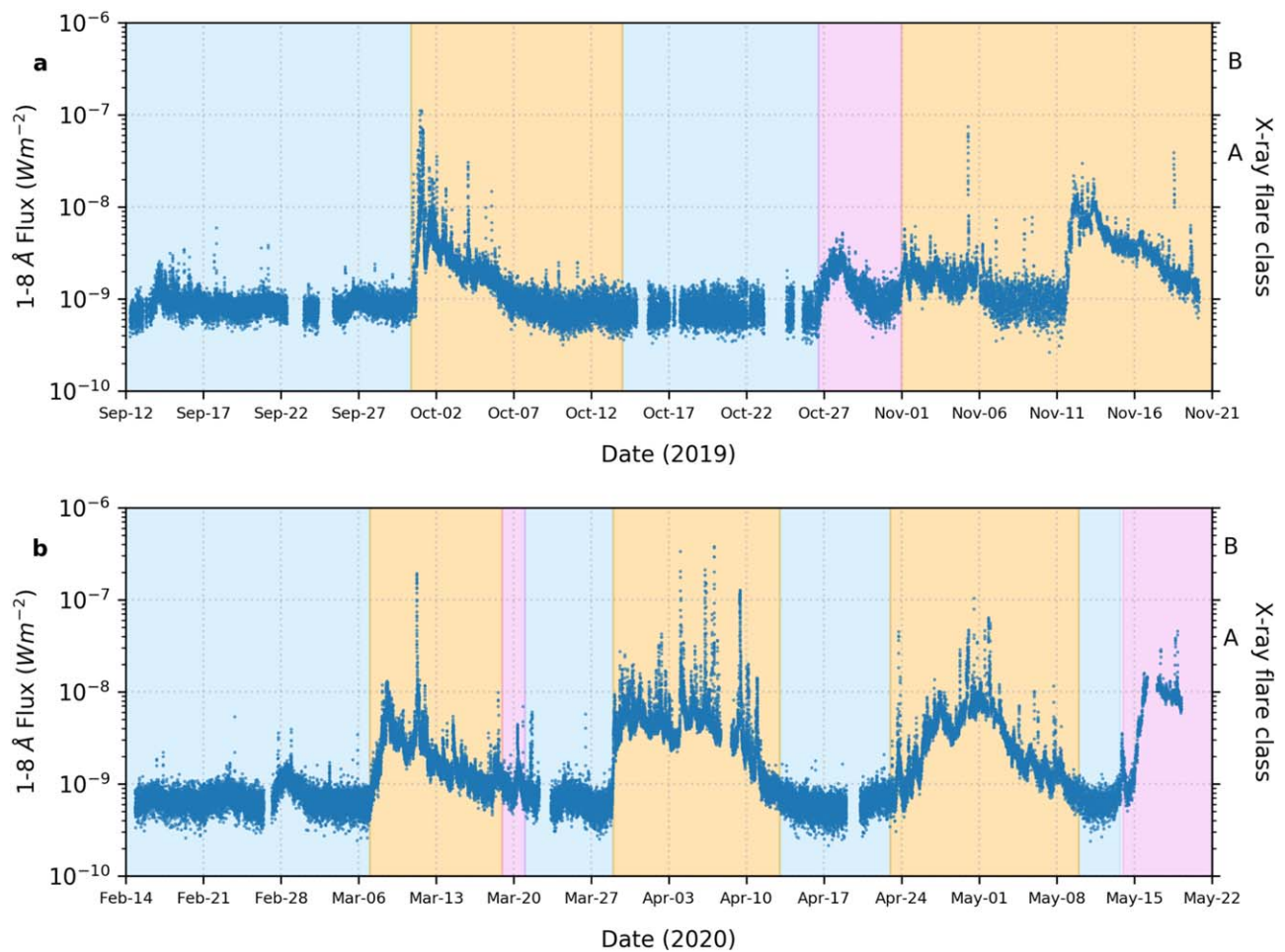


**Figure 1.** Solar X-ray flux in 1–8 Å (1.55–12.4 keV) from XSM observations for the two DD seasons. Background colors in the figure correspond to intervals with active regions (orange), enhanced X-ray activity (pink), and quiet-Sun observations (blue).

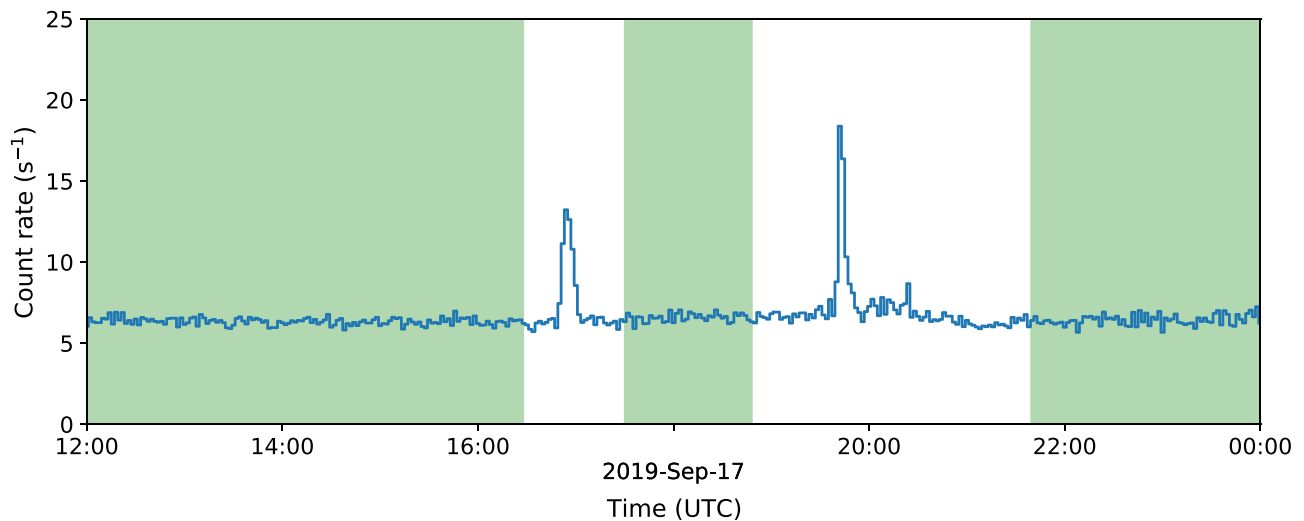


**Figure 2.** An example of selection of nonflaring quiescent periods based on the XSM light curve is shown. Durations shaded green, which exclude the flare duration with an additional margin before and after the flare, were selected as periods of observation of the quiescent corona and used for spectral analysis.

and line emission. It is imported as a local model into XSPEC, with temperature, emission measure, and abundances of elements from  $Z=2$  to 30 as model parameters. The details of the local model implementation will be discussed in a subsequent paper (B. Mondal et al. 2021, in preparation).

### 3. Results and Discussion

XSM observations during the first two DD seasons cover the period of possibly the lowest solar activity since the beginning of modern solar observations. The light curve shown in Figure 1 exhibits long periods when the solar X-ray intensity is

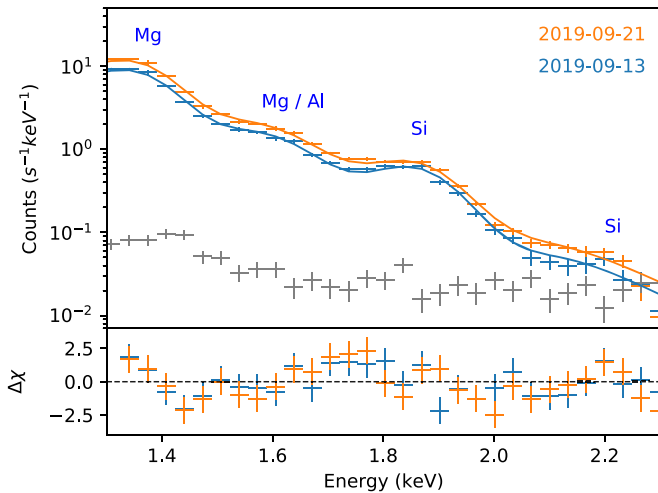


**Figure 3.** Soft X-ray spectra measured by the XSM for two representative days of quiet-Sun observations are shown. Solid lines represent the best-fit isothermal model and the residuals are shown in the bottom panel. Gray points correspond to nonsolar background spectrum.

very low but steady. It should be noted that the nonsolar X-ray background measured by XSM over the entire energy range is at least 35 times lower as discussed in Mithun et al. (2020). We find that the lowest solar X-ray flux measured by XSM in the GOES 1–8 Å band is about  $6 \times 10^{-10} \text{ W m}^{-2}$ , corresponding to the A0.06-class of solar activity, which is well below the sensitivity of the GOES-16 XRS instrument. Considering the fact that no active regions were present for an extended period during these observations, it is reasonable to assume that the solar corona was the quietest during these observations and that the XSM has measured the absolute floor level of the solar X-ray intensity.

We find that the solar X-ray spectra integrated over any of the selected 73 days is dominant over the nonsolar background spectrum up to 2.3 keV, as seen from Figure 3. The spectra show a clear signature of thermal X-ray emission with the line complexes of Mg, Al, and Si. Hence, we fit the spectra in the energy range of 1.3–2.3 keV with the CHIANTI based isothermal plasma emission model that allows us to constrain the temperature, emission measure, and abundances of Mg, Al, and Si. Abundances of all other elements, which do not contribute to the line emission in the energy range considered for fitting, are fixed to their known coronal abundance values. We verified that small changes in the abundances of these elements, or fixing them to their photospheric values, do not have any impact on the inferred parameters. Figure 3 shows the spectral fit results for two days of observation. It can be seen that the observed spectrum is well fitted with the isothermal model and similar fits were obtained for all spectra. One sigma errors on all free parameters of the model were also estimated using the standard procedure in XSPEC.

By analyzing integrated spectra for each day of the selected quiet-Sun periods, we obtained temperature, EM, and abundances of Mg, Al, and Si as shown in Figure 4. We find that the isothermal temperature and EM of the quiet corona typically remain constant around  $\sim 2.05 \text{ MK}$  and  $\sim 1.5 \times 10^{47} \text{ cm}^{-3}$ , respectively. However, there are small variations in temperature and emission measure, which are correlated with the variations in X-ray flux. Sylwester et al. (2019) reported isothermal temperatures of  $\sim 1.69 \text{ MK}$  for the

quiescent corona using X-ray spectroscopic observations in a similar energy range using SphinX observations during the 2009 solar minimum, which is lower than the estimates from XSM. They also noted that the isothermal fit does not explain the observed spectra completely and had shown the presence of higher-temperature components with differential emission measure (DEM) analysis, unlike in the present case where the XSM spectra in the range of 1.3–2.3 keV is consistent with isothermal models. One possible reason for the difference could be that the abundances were frozen to coronal values in the case of SphinX analysis as they could not be constrained due to relatively poorer energy resolution, whereas the abundances could be fitted in the case of XSM observations.

The estimated abundances for the low FIP elements Mg, Al, and Si are most of the time higher than the photospheric values. However, compared to various coronal abundance values reported in the literature for active regions (Feldman 1992; Fludra & Schmelz 1999; Schmelz et al. 2012), our average values are 20%–60% lower for Mg and Si. Whereas, for Al, the present derived values are  $\sim 30\%$  lower than the Feldman (1992) value, but comparable with the others. We note that the contribution of Al in the energy band comprising Al lines is about 10%, resulting in a lower sensitivity to Al abundance as reflected in relatively larger error bars. In order to establish the robustness of the measurements of Al abundances as well as other parameters, we carried out Markov Chain Monte Carlo (MCMC) analysis and the results are shown in Figure 5. These results clearly show that all parameters including Al abundances are reasonably well constrained. To verify the consistency of our elemental abundance estimates over multiple days, we carried out analysis of the spectra integrated over 2–4 days. These results are also shown in Figure 4. We also carried out similar analysis for the spectra integrated over the whole duration of the respective quiet period (represented by blue lines in Figure 4) and the results are given in Table 1. We note that the abundance of Si during the period of October 14–26 is anomalously low compared to other selected periods and further investigations are needed to identify the reason behind this.

In order to investigate the reason for the different FIP bias in the XSM observations, we checked the X-ray images from the XRT on board Hinode (Golub et al. 2007) taken with the Be-thin filter, which has a similar efficiency as the XSM at lower energies. The X-ray images during the selected days show that most of the X-ray emission observed in the XSM energy range arises from a few hot spots, known as X-ray bright points (XBPs), first reported by Golub et al. (1974). To verify this further, we simulated the expected XSM count rate from the quiet coronal region excluding any XBPs using the DEM from Brooks et al. (2009). We generated synthetic spectra with CHIANTI using this DEM and convolved it with the XSM detector response matrix to obtain the expected count rate. We find that the X-ray emission from the diffuse corona having peak temperature around 1 MK and photospheric elemental abundances can account for only 30%–50% of the observed count rate, suggesting that the majority of X-ray emission observed by XSM originates in XBPs. This is further confirmed by the fact that the overall temperature of around  $\sim 2 \text{ MK}$ , as observed by XSM, is much higher than that known for the quiet and diffuse corona. Observations with Hinode XRT have also reported temperatures ranging from 1.1 to 3.4 MK for

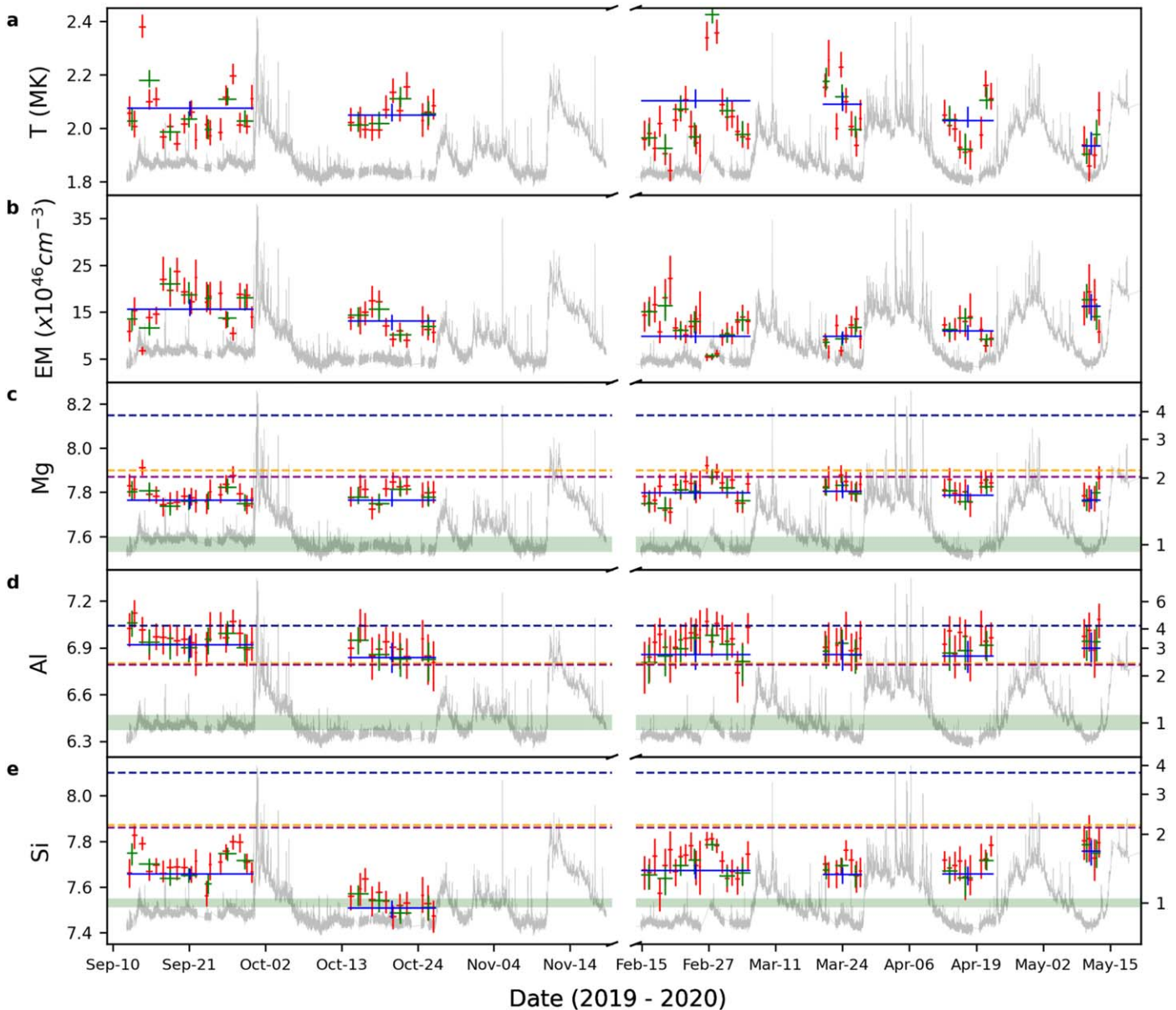


**Figure 4.** The five panels show the results of the spectral fitting, viz. temperature (a), EM (b), as well as the absolute abundances of Mg (c), Al (d), and Si (e) in logarithmic scale with  $A(H) = 12$ . The red, green, and blue points represent the best-fit parameters obtained from the spectra integrated over one day, multiple days (2–4 days), and each quiet period, respectively. The  $y$ -error bars represent  $1\sigma$  uncertainty for each parameter, whereas the  $x$ -error bars represent the duration over which a given spectrum is integrated. XSM light curves for the entire duration are shown in gray in the background. For a quick comparison with the reported values of abundances for these elements, the corresponding panels (c)–(e) also show lines representing active region values reported by Feldman (1992) (navy blue), Fludra & Schmelz (1999) (orange), and Schmelz et al. (2012) (purple). The range of photospheric abundances from various authors compiled in the CHIANTI database are shown as green bands. The right  $y$ -axis in panels (c)–(e) shows the FIP bias values for the respective elements with respect to average photospheric abundances.

XBPs (Kariyappa et al. 2011). Thus, we conclude that the intermediate FIP bias observed by XSM most likely corresponds to the XBPs. To the best of our knowledge, this is the first report of the elemental abundances for XBPs having a temperature of  $\sim 2$  MK. According to present theoretical understanding of FIP bias (Laming 2009; Dahlburg et al. 2016), the XBPs having intermediate field strengths and temperatures are expected to have intermediate FIP bias; however, there has been no observational evidence so far supporting this conjecture. Our observations confirm this expectation for the first time with robust abundance measurements over an extended period.

#### 4. Summary

In the Sun-as-a-star mode observations, carrying out prolonged study of the quiet solar corona is often challenging because of the presence of bright active regions that typically occur throughout the solar cycle. The 2019–2020 solar minimum offered such an opportunity for extended quiet corona observations when there were no active regions present on the visible solar disk. The XSM on board Chandrayaan-2 was the only X-ray spectrometer operational during a good part of this minimum and optimally utilized this opportunity. It measured possibly the lowest intensity of the coronal X-rays with high significance and we find that the

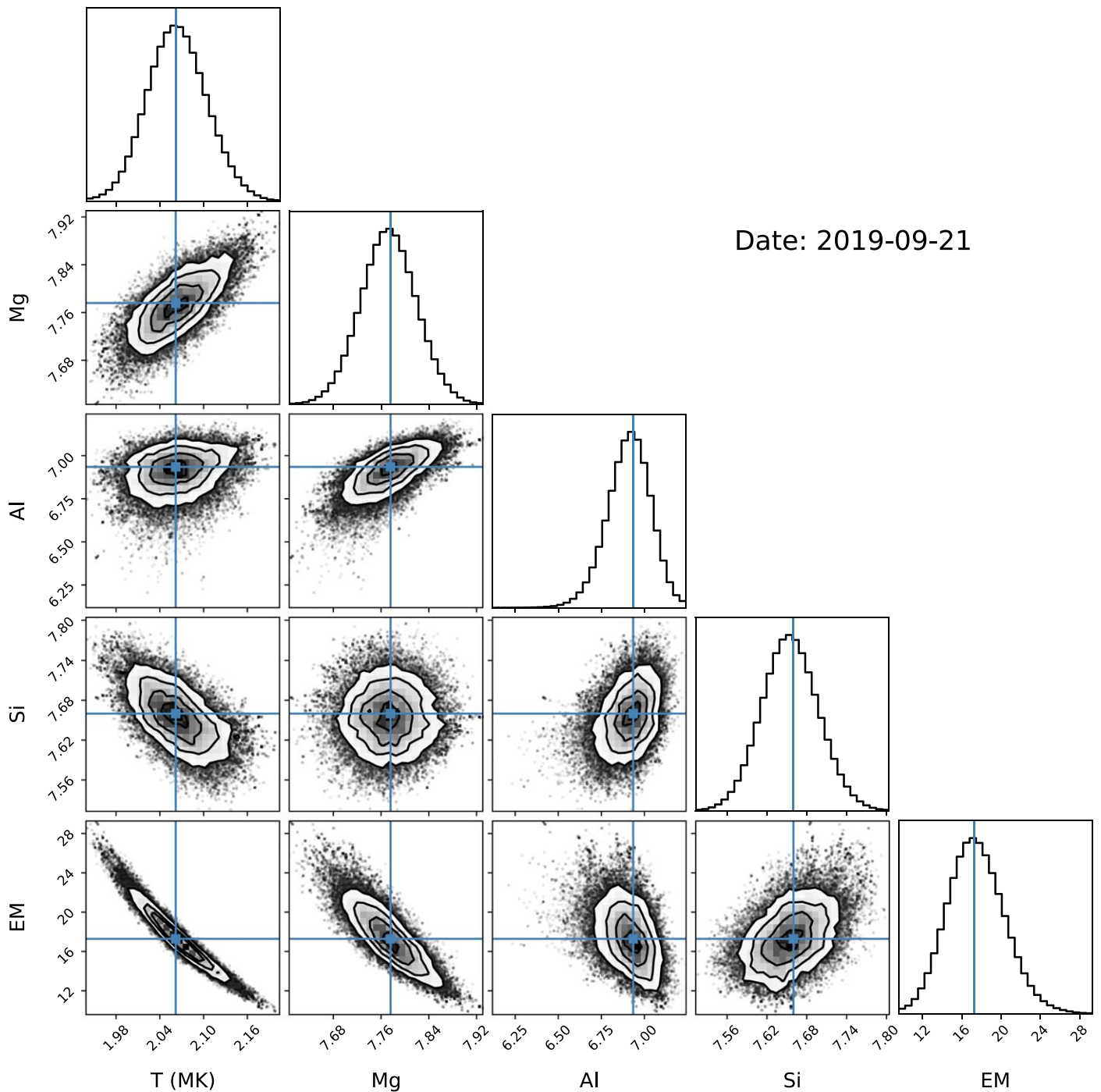


**Figure 5.** Corner plot showing results of MCMC analysis of representative quiet-Sun spectrum on 2019 September 21. The histograms represent marginalized distributions of each parameter. Correlations between all pairs of parameters are shown in the scatterplots overlaid by the contours corresponding to 1, 2, and  $3\sigma$  levels. Best-fit parameters are shown by the blue lines.

(The complete figure set (73 images) is available.)

bulk of this X-ray emission likely originates in the XBPs. Detailed spectroscopic analysis of these observations show that plasma temperature in the XBPs is around  $\sim 2$  MK and that the abundances of the low FIP elements in the XBPs are at a level intermediate to their photospheric and coronal abundances. Our results are consistent with the ponderomotive force model, which is widely considered to be responsible for the coronal FIP bias.

Such a rare opportunity is not likely to be available at least for a decade, until the end of Solar Cycle 25. Though the XSM may not be operational during the next solar minimum, it will observe the Sun at least during the rising phase of Solar Cycle 25. Thus, with its superior sensitivity, energy resolution, and time cadence, XSM is expected to provide rich observations having far-reaching consequences for the study of highly dynamic Sun.

**Table 1**  
Quiet-Sun Parameters Obtained from XSM Spectra Integrated over Each Quiet Period



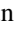






Observation Period	$T$ (MK)	EM ( $10^{46} \text{ cm}^{-3}$ )	Mg	Al	Si
2019 Sep 12–Sep 30	$2.07^{+0.02}_{-0.02}$	$15.6^{+2.08}_{-1.46}$	$7.76^{+0.02}_{-0.03}$	$6.92^{+0.06}_{-0.08}$	$7.65^{+0.02}_{-0.02}$
2019 Oct 14–Oct 26	$2.05^{+0.04}_{-0.02}$	$13.1^{+1.36}_{-2.04}$	$7.76^{+0.04}_{-0.02}$	$6.83^{+0.09}_{-0.09}$	$7.50^{+0.03}_{-0.04}$
2020 Feb 14–Mar 7	$2.10^{+0.04}_{-0.02}$	$9.86^{+1.07}_{-1.49}$	$7.79^{+0.04}_{-0.03}$	$6.85^{+0.09}_{-0.09}$	$7.67^{+0.02}_{-0.03}$
2020 Mar 21–Mar 29	$2.09^{+0.04}_{-0.02}$	$9.81^{+1.09}_{-1.54}$	$7.80^{+0.04}_{-0.03}$	$6.85^{+0.09}_{-0.10}$	$7.65^{+0.02}_{-0.04}$
2020 Apr 13–Apr 23	$2.02^{+0.05}_{-0.02}$	$10.9^{+1.24}_{-1.99}$	$7.78^{+0.04}_{-0.03}$	$6.84^{+0.09}_{-0.10}$	$7.65^{+0.03}_{-0.05}$
2020 May 10–May 13	$1.93^{+0.05}_{-0.03}$	$16.3^{+2.64}_{-3.13}$	$7.76^{+0.04}_{-0.04}$	$6.89^{+0.09}_{-0.11}$	$7.75^{+0.04}_{-0.06}$

XSM was designed and developed by the Physical Research Laboratory (PRL), Ahmedabad with support from the Space Application Centre (SAC), Ahmedabad, the U. R. Rao Satellite Centre (URSC), Bengaluru, and the Laboratory for Electro-Optics Systems (LEOS), Bengaluru. We thank various facilities and the technical teams of all the above centers and Chandrayaan-2 project, mission operations, and ground segment teams for their support. The Chandrayaan-2 mission is funded and managed by the Indian Space Research Organisation (ISRO). Research at PRL is supported by the Department of Space, Govt. of India. We gratefully acknowledge G. Del-Zanna, H. E. Mason, and U. Mitra Kraev for their help with the use of CHIANTI as well as very helpful discussions, facilitated through Royal Society Grant No. IESR2\170199.

*Facility:* Chandrayaan-2 (XSM).

*Software:* XSMDAS (Mithun et al. 2021a), XSPEC (Arnaud 1996), Python, Matplotlib, Corner.py (Foreman-Mackey 2016).

### ORCID iDs

Santosh V. Vadawale  <https://orcid.org/0000-0002-2050-0913>  
 Biswajit Mondal  <https://orcid.org/0000-0002-7020-2826>  
 N. P. S. Mithun  <https://orcid.org/0000-0003-3431-6110>  
 Aveek Sarkar  <https://orcid.org/0000-0002-4781-5798>  
 P. Janardhan  <https://orcid.org/0000-0003-2504-2576>  
 Bhuwan Joshi  <https://orcid.org/0000-0001-5042-2170>  
 Anil Bhardwaj  <https://orcid.org/0000-0003-1693-453X>  
 Arpit R. Patel  <https://orcid.org/0000-0002-0929-1401>  
 Shiv Kumar Goyal  <https://orcid.org/0000-0002-3153-537X>

### References

Arnaud, K. A. 1996, in ASP Conf. Ser. 101, *Astronomical Data Analysis Software and Systems V*, ed. G. H. Jacoby & J. Barnes (San Francisco, CA: ASP), 17  
 Brooks, D. H., Baker, D., van Driel-Gesztelyi, L., & Warren, H. P. 2017, *NatCo*, 8, 183  
 Brooks, D. H., Warren, H. P., Williams, D. R., & Watanabe, T. 2009, *ApJ*, 705, 1522  
 Caspi, A., Woods, T. N., & Warren, H. P. 2015, *ApJL*, 802, L2  
 Dahlburg, R. B., Laming, J. M., Taylor, B. D., & Obenshain, K. 2016, *ApJ*, 831, 160

Del Zanna, G. 2019, *A&A*, 624, A36  
 Del Zanna, G., & Mason, H. E. 2014, *A&A*, 565, A14  
 Del Zanna, G., & Mason, H. E. 2018, *LRSP*, 15, 5  
 Dennis, B. R., Phillips, K. J. H., Schwartz, R. A., et al. 2015, *ApJ*, 803, 67  
 Dere, K. P., Del Zanna, G., Young, P. R., Landi, E., & Sutherland, R. S. 2019, *ApJS*, 241, 22  
 Dere, K. P., Landi, E., Mason, H. E., Monsignori Fossi, B. C., & Young, P. R. 1997, *A&AS*, 125, 149  
 Doschek, G. A., & Warren, H. P. 2019, *ApJ*, 884, 158  
 Feldman, U. 1992, *PhysS*, 46, 202  
 Feldman, U., & Laming, J. M. 2000, *PhysS*, 61, 222  
 Feldman, U., & Widing, K. G. 1993, *ApJ*, 414, 381  
 Feldman, U., & Widing, K. G. 2003, *SSRv*, 107, 665  
 Fludra, A., & Schmelz, J. T. 1999, *A&A*, 348, 286  
 Foreman-Mackey, D. 2016, *JOSS*, 1, 24  
 Golub, L., Deluca, E., Austin, G., et al. 2007, *SoPh*, 243, 63  
 Golub, L., Krieger, A. S., Silk, J. K., Timothy, A. F., & Vaiana, G. S. 1974, *ApJL*, 189, L93  
 Janardhan, P., Bisoi, S. K., Ananthkrishnan, S., et al. 2015, *JGRA*, 120, 5306  
 Janardhan, P., Bisoi, S. K., Ananthkrishnan, S., Tokumaru, M., & Fujiki, K. 2011, *GeoRL*, 38, L20108  
 Kariyappa, R., Deluca, E. E., Saar, S. H., et al. 2011, *A&A*, 526, A78  
 Laming, J. M. 2004, *ApJ*, 614, 1063  
 Laming, J. M. 2009, *ApJ*, 695, 954  
 Laming, J. M. 2015, *LRSP*, 12, 2  
 Mason, H. E. 1975, *MNRAS*, 171, 119  
 Meyer, J. P. 1985, *ApJS*, 57, 173  
 Mithun, N. P. S., Vadawale, S. V., Patel, A. R., et al. 2021a, *A&C*, 34, 100449  
 Mithun, N. P. S., Vadawale, S. V., Sarkar, A., et al. 2020, *SoPh*, 295, 139  
 Mithun, N. P. S., Vadawale, S. V., Shanmugam, M., et al. 2021b, *ExA*, 51, 33  
 Moore, C. S., Caspi, A., Woods, T. N., et al. 2018, *SoPh*, 293, 21  
 Narendranath, S., Sreekumar, P., Alha, L., et al. 2014, *SoPh*, 289, 1585  
 Narendranath, S., Sreekumar, P., Pillai, N. S., et al. 2020, *SoPh*, 295, 175  
 Pipin, V. V., & Tomozov, V. M. 2018, *ARep*, 62, 281  
 Pottasch, S. R. 1963, *ApJ*, 137, 945  
 Saba, J. L. R. 1995, *AdSpR*, 15, 13  
 Schmelz, J. T., Reames, D. V., von Steiger, R., & Basu, S. 2012, *ApJ*, 755, 33  
 Schwab, B. D., Sewell, R. H. A., Woods, T. N., et al. 2020, *ApJ*, 904, 20  
 Shanmugam, M., Vadawale, S. V., Patel, A. R., et al. 2020, *CSci*, 118, 45  
 Sylwester, B., Sylwester, J., Siarkowski, M., et al. 2019, *SoPh*, 294, 176  
 Vadawale, S. V., Mithun, N. P. S., Mondal, B., et al. 2021, *ApJL*, 912  
 Vadawale, S. V., Shanmugam, M., Acharya, Y. B., et al. 2014, *AdSpR*, 54, 2021  
 Vanitha, M., Veeramuthuvel, P., Kalpana, K., & Nagesh, G. 2020, *LPSC*, 51, 1994  
 Walker, A. B. C., J 1972, *SSRv*, 13, 672  
 Walker, A. B. C., Ruge, J., & Weiss, K., H. R. 1974a, *ApJ*, 188, 423  
 Walker, A. B. C., J., Ruge, H. R., & Weiss, K. 1974b, *ApJ*, 192, 169  
 Warren, H. P. 2014, *ApJL*, 786, L2